metals

MDPI

Article

Failure Analysis of the Half-Shafts Belonging to a Three-Wheeled Electric Vehicle

Inês Mendes [1], J. Henrique Lopes [1,2], Eduardo Matos Almas [1] and Luís Reis [1,2,*]

[1] Instituto Superior Técnico, Universidade de Lisboa, Av. Rovisco Pais 1, 1049-001 Lisboa, Portugal; ines.s.mendes@tecnico.ulisboa.pt (I.M.); henrique.lopes@tecnico.ulisboa.pt (J.H.L.); emalmas@dem.ist.utl.pt (E.M.A.)

[2] IDMEC, Instituto Superior Técnico, Universidade de Lisboa, Av. Rovisco Pais, 1049-001 Lisboa, Portugal

* Correspondence: luis.g.reis@tecnico.ulisboa.pt

Abstract: In the electric vehicles studied, the driven wheels and the differential, which are responsible for the transfer of power and rotational motion, are connected by half-shafts. The failure of two half-shafts in the rear gearbox of a three-wheeled electric vehicle, popularly known as a Tuk Tuk, is examined and evaluated in this research. Therefore, the primary goal of this work is to look at the factors that contribute to the failure of the aforementioned components. Visual examination and fractographic analysis were performed utilizing optical and scanning electron microscopes to investigate the half-shafts' mode of failure. Samples from both half-shafts were obtained for tensile testing, metallographic examination, chemical composition analysis, and fracture surface analysis. According to visual examination, reversed bending fatigue, occurring simultaneously with torsion loading, caused the fracture in the half-shaft to the left of the differential (rear view). Analysis of the fracture surface of the half-shaft to the right of the differential revealed that it resulted mainly from bending fatigue loading. Moreover, regarding the mechanical design safety of the half-shafts, calculations were performed considering different trajectories, limit speeds, and different design criteria. Finally, some recommendations are drawn to improve the design safety of this mechanical component.

Keywords: shafts; half-shafts; electric vehicle; fatigue failure; design criteria

check for updates

Citation: Mendes, I.; Lopes, J.H.; Almas, E.M.; Reis, L. Failure Analysis of the Half-Shafts Belonging to a Three-Wheeled Electric Vehicle. *Metals* **2024**, *14*, 727. https://doi.org/10.3390/met14060727

Academic Editors: Zhixin Zhan and Chuanqi Liu

Received: 3 April 2024
Revised: 11 June 2024
Accepted: 16 June 2024
Published: 19 June 2024

Copyright: © 2024 by the authors. Licensee MDPI, Basel, Switzerland. This article is an open access article distributed under the terms and conditions of the Creative Commons Attribution (CC BY) license (https://creativecommons.org/licenses/by/4.0/).

1. Introduction

Shafts are key components of mechanical equipment in several industries [1]. They are applied in the automotive [2,3], railway [4], and aerospace [5] industries. They are responsible for transmitting the power that originates from the engine to the wheel(s), rotor, or propeller.

According to Asi, because of the nature of their purpose, rotating parts are most vulnerable to fatigue failure, which often takes the form of torsional bending, rotating bending, or reversed bending [6,7]. Particularly, half-shafts or axle-shafts, found in four- or three-wheeled vehicles, are responsible for transmitting the torque from the differential to the wheels. Bayrakceken et al. [8] have demonstrated the crack origin in the highly stressed regions of a vehicle's half-shaft through finite element analysis (FEA). The modal analysis to predict the failure of the rear axle of a vehicle performed in Verma et al. [9] also shows that the spline portion is prone to failure. Experimental results show similar results to those of the torsion fatigue tests conducted in [10] on 15 different front half-shafts of an existing car, showed that cracks initiate at the spline profile due to the high stress concentration factor at that location. Similarly, the fractured half-shaft component belonging to the transmission system of an SAE racing car occurred on account of the torsional fatigue crack propagation and overload ductile fracture at the spline section [11]. More recently, Alberti et al. [12] have presented a design algorithm to evaluate the fatigue damage in automotive mechanical components.

Fracture due to fatigue begins as a microcrack inside the crystallographic planes with high shear stress, followed by the crack spreading in a perpendicular direction to the applied load [13]; this causes rapid spreading that eventually results in a rupture [14–17]. In research on the causes of shaft failures for rotary machines reported by Bonnett [18], ductile fracture, brittle fracture, and creep are recognized and classified. One of the main characteristics of the fatigue fracture surface is the beach marks as well as the fatigue striations; these are not observed in the region over which the rapid failure occurs. This characteristic can be ductile or brittle and there will be evidence of plastic deformation for ductile failure [19–21] and its absence for brittle failure [22,23]. By observing the fracture surface, it is possible to obtain information about the applied forces as well as their magnitude. When the magnitude of the loading is reduced, the area occupied by the fatigue zone is greater than the area of the instantaneous fracture zone; in the case of high magnitudes, the opposite happens [24–28].

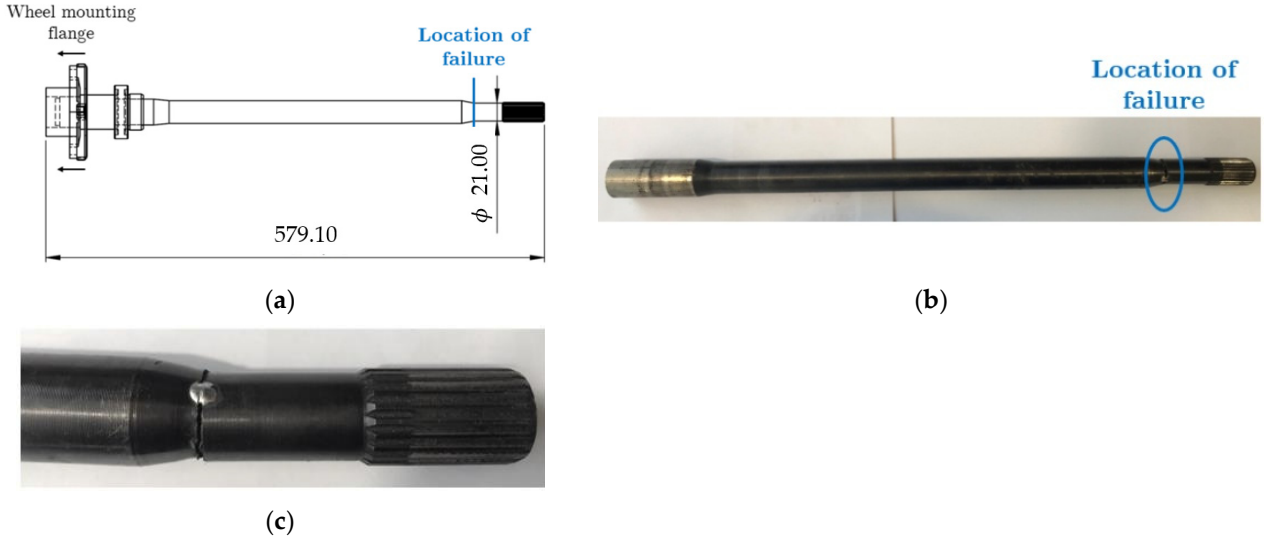
In this paper, the failures of two real components of an electric vehicle are analyzed using experimental and analytical methods. The root of the respective failures was determined and based on the in-service loads of this type of vehicle; some good engineering practices are recommended. Concerning its structure, in Section 1, this study investigates the failure of the half-shafts of an unknown material in the rear gearbox of a three-wheeled electric vehicle (Tuk Tuk). Section 2 details the experimental procedures and techniques used in the study. Section 3 presents the findings from visual observations, fractography, microstructural analysis, and chemical analysis. In Section 4, the results are analyzed, and the safety factor of the half-shafts is determined. Finally, Section 5 summarizes the key findings and provides valuable recommendations to improve the design safety of the parts.

2. Materials and Methods

The components studied in this work belong to an e-TUK Limo vehicle [29]; please see Figure 1. It contains an electric motor, and under normal working circumstances, it produces 7.0 kW of engine power at 3100 rpm and 21.56 N.m of peak torque on the drive shaft. The gear train, which has the electric motor's input shaft directly coupled to it and the gear train's output shafts corresponding to the rear transmission system's half-shafts, transmits the power from the electric motor to the differential. The business TUK ON ME (Lisbon, Portugal) purchased the e-TUK type Limo in 2015. A year after the acquisition (about 15,000 km traveled), the rear-wheel drive half-shafts of the three-wheeled electric vehicle (3WEV) fractured. The fractured half-shafts used for carrying out this study are shown in Figures 2b and 3b. Figure 2a shows the location of the fracture on the half-shaft mounted left of the differential (in the rear view of the vehicle), designated as half-shaft 1. The failure occurred in the diameter transition, on the side that is geared with the planetary gear of the differential. Figure 3a shows the fracture location on the half-shaft mounted right of the differential (in the rear view of the vehicle), designated as half-shaft 2. The failure occurred in the diameter transition, on the side of the tire mounting flange.



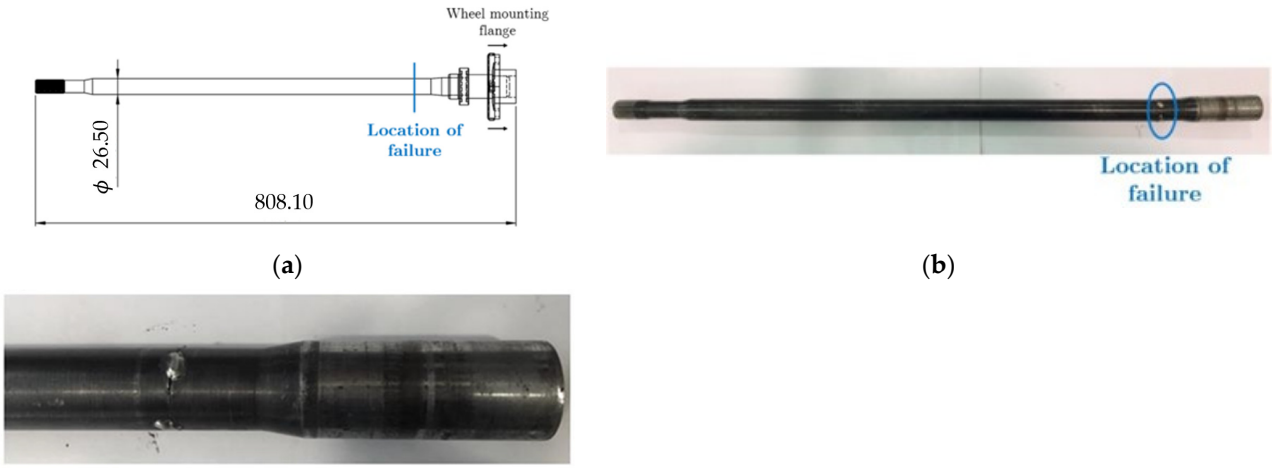
Figure 1. Vehicle under study, e-Tuk Limo reprinted from Ref. [29].



(**a**) (**b**)

(**c**)

Figure 2. (**a**) Diagram of half-shaft 1, showing the position of the fracture; (**b**) half-shaft used for the study; (**c**) detail of the failure location (dimensions in mm).



(**a**) (**b**)

(**c**)

Figure 3. (**a**) Diagram of half-shaft 2, showing the position of the fracture; (**b**) half-shaft used for the study; (**c**) detail of the failure location (dimensions in mm).

Both half-shafts were visually inspected for a general idea of the type of fracture; more precisely, to determine its location, shape, and size, and the characteristics of the fracture surface.

In order to determine the main mechanical properties of the unknown materials belonging to both half-shafts, two test specimens measuring 6.0 mm in diameter and 42.5 mm in length in the gauge length (1A, 1B, 2A, and 2B; please see Figure 4a,c) were machined according to ASTM E8 [30]; this was conducted close to the fracture section of each half-shaft according to the axial direction for the tensile test. Both half-shafts have a 26.50 mm diameter at the point where the specimens were taken. The test was performed at a rate of 2.0 mm/min on an Instron 3369 (Norwood, MA, USA) universal electromechanical testing machine using also the Instron 2630-100 strain gauge (Norwood, MA, USA). The laboratory was at 20 °C and 50% humidity.

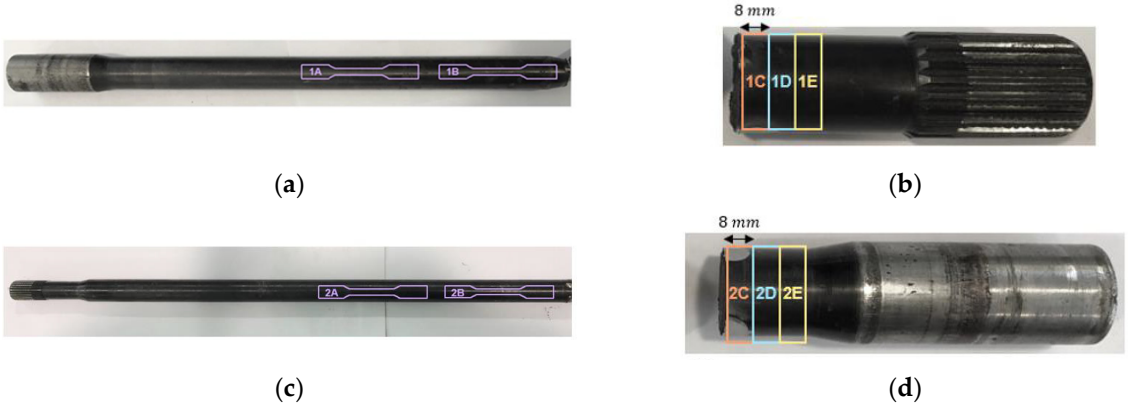


Figure 4. (**a**) Tensile specimens from half-shaft 1; (**b**) samples (1C, 1D, 1E) from half-shaft 1 to SEM inspection; (**c**) tensile specimens from half-shaft 2; (**d**) samples (2C, 2D, 2E) from half-shaft 2 to SEM inspection.

To characterize the fracture surface and identify fracture mechanisms, three 8 mm thickness cylinders (1C, 1D, 1E, 2C, 2D, and 2E diameters, equal to 20.0 mm; please see Figure 4b,d) were taken from each half-shaft that had a fracture surface, and they were examined using a Hitachi S 2400 SEM (Tokyo, Japan) with an EDS detector to provide fractographic pictures of the surface and its chemical composition.

A microstructure examination was also performed. The microstructure of the material was obtained after sanding, polishing, and contrasting the sample with 4% Nital for 3 s using the Olympus PMG3 microscope (Tokyo, Japan), the Olympus U-PMTVC microscope camera (Tokyo, Japan), and a scanning electron microscope (SEM).

In order to consider the loading conditions on the half-shafts and their influence on their failure, two potential situations were considered: (a) when the vehicle travels in a straight line; (b) when the vehicle takes tight curves, as these are the most frequent road sections in the circuits traveled by the 3WEV. The objective is to characterize and assess the stresses in the half-shafts, namely on those sections where the half-shafts fractured, ending with the determination of the fatigue safety coefficient by well-known fatigue criteria. Finally, concerning the aforementioned factors, some recommendations are drawn in order to improve the design safety of this mechanical component.

3. Results

3.1. Visual Observations and Fractography

The fracture surface of half-shaft 1 was visually observed by both optical observation and SEM. The objective is to identify features/defects in the material surface that enable evidence to be found of the origin of the failure. From Figure 5, it is possible to identify that cracking occurred in multiple places (see red lines, circumscribing the main cracking zones), meaning that the applied loads were high and close to the outer surface due to the influence of the type of loading (bending and/or torsion moment). The final fracture zone (FFZ) that appears in the center of the sample is relatively large, meaning that a medium-/high-magnitude loading was applied in the half-shaft; their features imply a strong influence on the torque (mode III). Based on the identified features of the fracture surface, it appears to correspond to a rotating bending plus torsion fatigue fracture, where multiple crack initiation sites are visible.

This fracture surface was examined to identify the fracture mechanisms and their micro characteristics. Figure 6 depicts a few initial sites of cracking, also known as ratchet marks (fatigue fracture indicators, inside the red line), which are formed when many sources of fatigue fractures are combined. Material that had been torn and wrenched away was visible in the final fracture zone (please see Figure 7), due to the presence of high loads on the half-shaft. In Figure 7b, the presence of machined marks, indicated by B, characterize

the bad surface finishing of the half-shaft close to the diameter transition; these certainly contributed to the root cause of the failure.

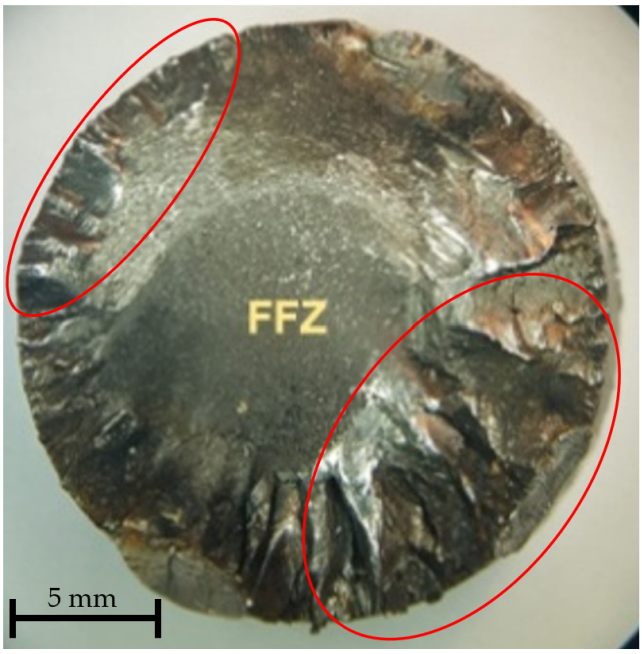


Figure 5. Appearance of half-shaft 1's fracture surface, showing the final fracture zone (FFZ).

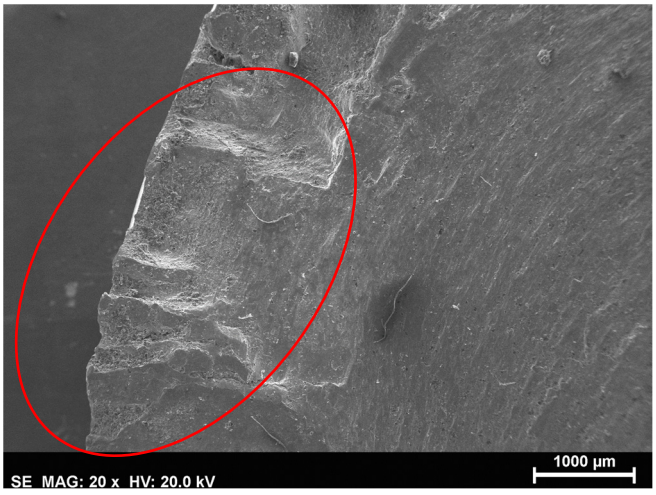
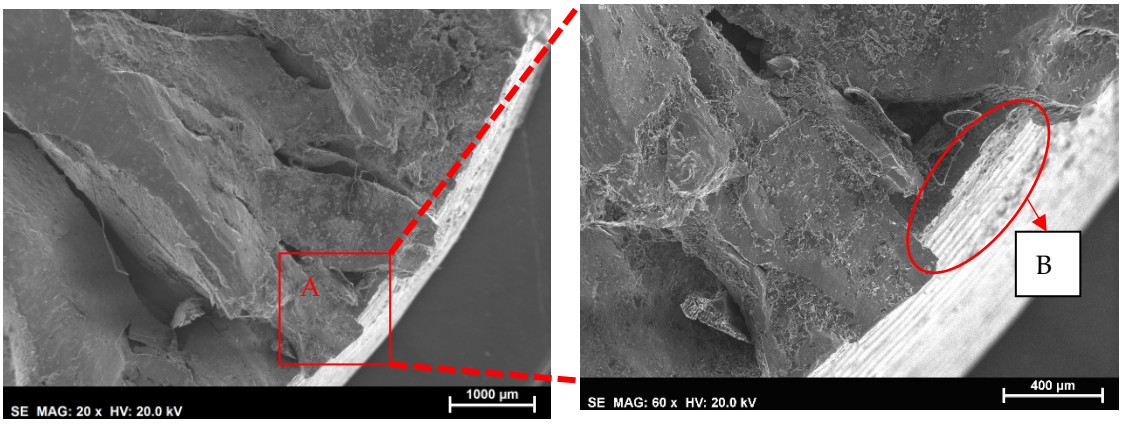


Figure 6. Ratchet marks on the fracture surface of half-shaft 1.

Figure 8 presents the fracture surface of half-shaft 2 through observation by optical microscopy with low magnification. Based on this observation, it is possible to identify different regions on the fracture surface morphology: the crack initiation point (indicated by A); the fatigue crack propagation region (indicated by FZ), where beach marks are visible; the final fracture zone (indicated by FFZ). According to the fracture surface's features, it appears to be a rotating bending fatigue fracture brought on by a medium–high-magnitude loading near a moderate stress concentration (please refer to Figure 3c). In the fatigue crack propagation zone (FZ), beach marks are a sign of the corresponding fatigue failure mechanism.



(**a**) (**b**)

Figure 7. (**a**) Fracture surface morphology of half-shaft 1; (**b**) detail of location A (**a**) and identification of machined marks at location B.

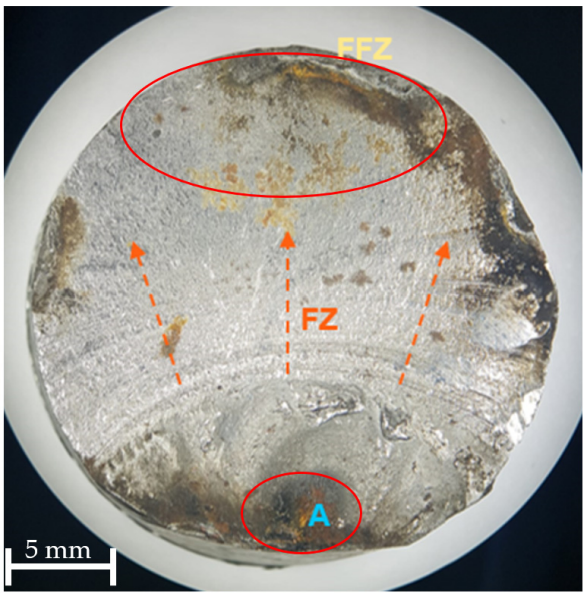
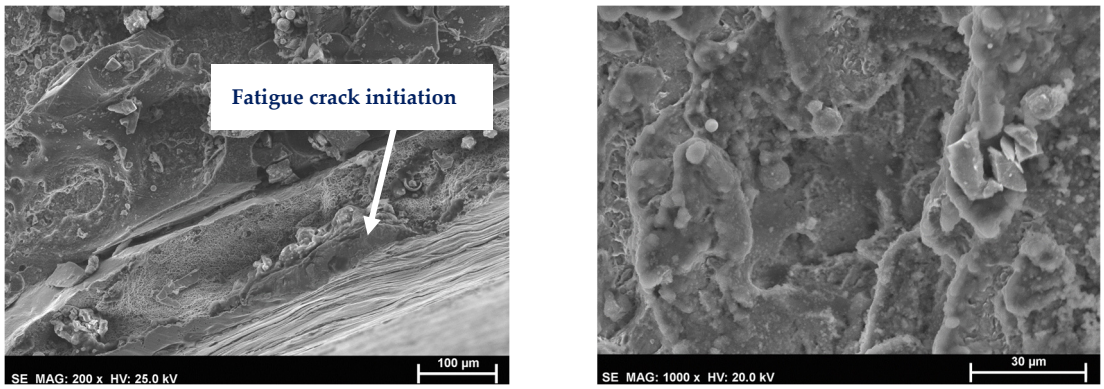


Figure 8. Identification of the crack-initiation zone (A), the fatigue crack propagation zone (FZ), and the final fracture zone (FFZ) on the fracture surface of half-shaft 2.

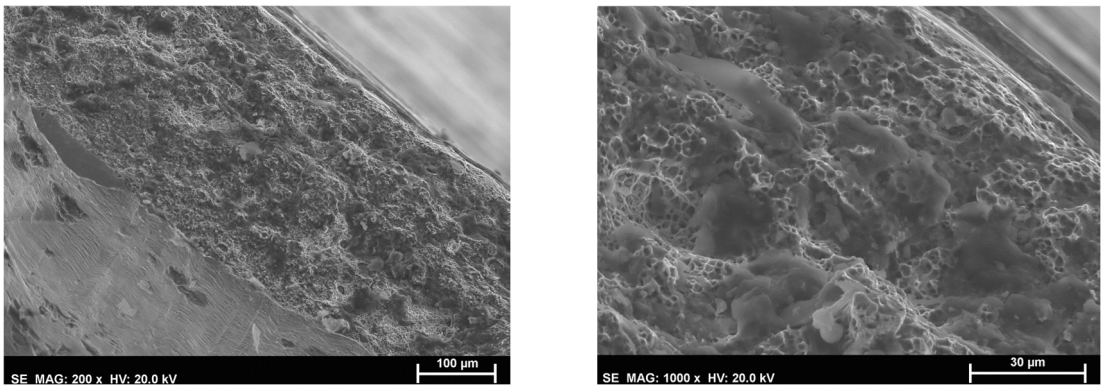
As in the case of half-shaft 1, the fracture surface of half-shaft 2 was examined by SEM to identify the fracture mechanisms and their micro characteristics. The magnification of the crack-initiation zone allows us to identify the fatigue crack initiation (please, see Figure 9a) and intercrystalline cracking (Figure 9b). A lot of debris can be seen, including secondary cracks, faces where the material was pulled out, and a large tear, possibly due to the high load applied in this section of the half-shaft. Microcavities and dimples may be seen in the fractographic picture of the final fracture zone (Figure 10); these are connected to a ductile fracture at the ultimate rupture.

Considering the component under study and the type of in-service loads which it is subject to for most of its service time, the application of thermal or mechanical treatments can improve the mechanical response of this material, particularly through treatments that introduce residual compressive stresses on the surface.



(**a**) (**b**)

Figure 9. Enlargement of the crack-initiation zone, location A in Figure 8, visualizing the following: (**a**) fatigue crack initiation; (**b**) intercrystalline cracking.

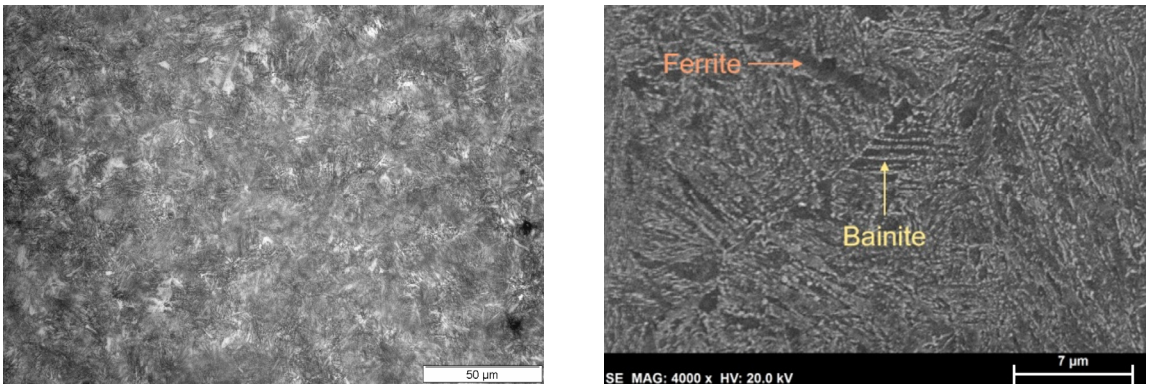


(**a**) (**b**)

Figure 10. (**a**) Enlargement of fracture surface morphology of FFZ; (**b**) detail of enlargement of FFZ.

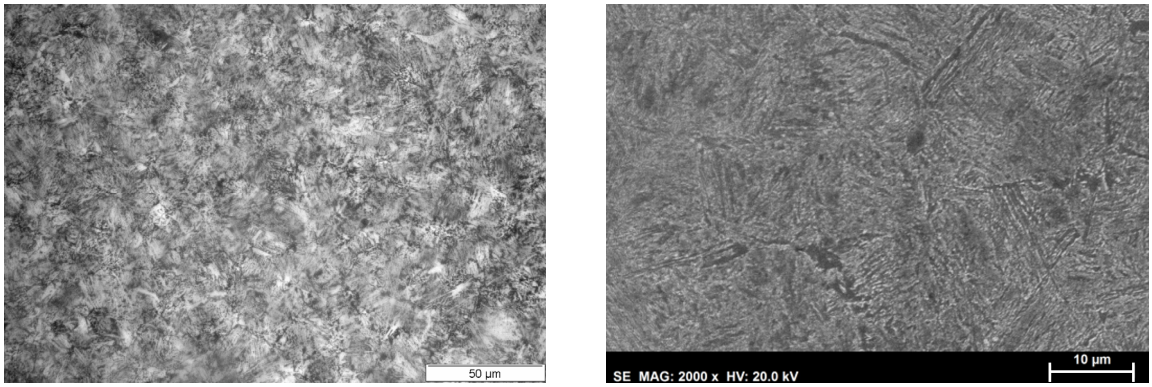
3.2. Microstructural Analysis

Figures 11 and 12 illustrate the microstructure from the half-shaft 1 sample and the half-shaft 2 sample, respectively. The microstructures of the fractured half-shafts are similar and correspond to a bainitic structure, where the ferrite microstructure is also present (see Figure 11b). These microstructures were obtained from samples taken close to the fracture sections (samples 1D and 2D, Figure 4) of each half-shaft (see Figures 4b and 4d, respectively). A sweep was performed over the entire surface of the samples, and the results were similar.



(**a**) (**b**)

Figure 11. Half-shaft 1 microstructure: (**a**) Olympus PMG3 microscope with ×500 magnification; (**b**) SEM S-2400 with ×4000 magnification.

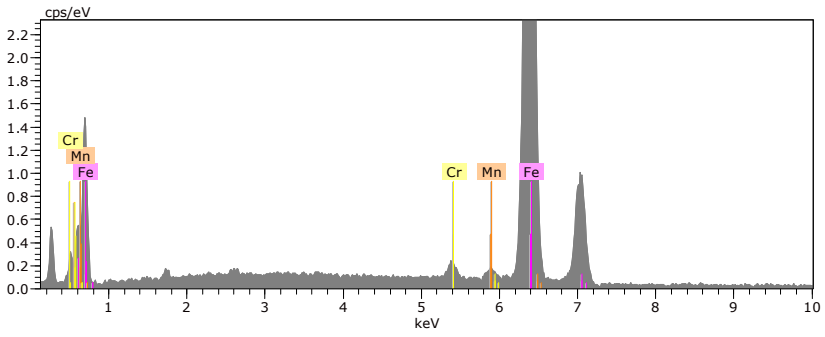


(**a**) (**b**)

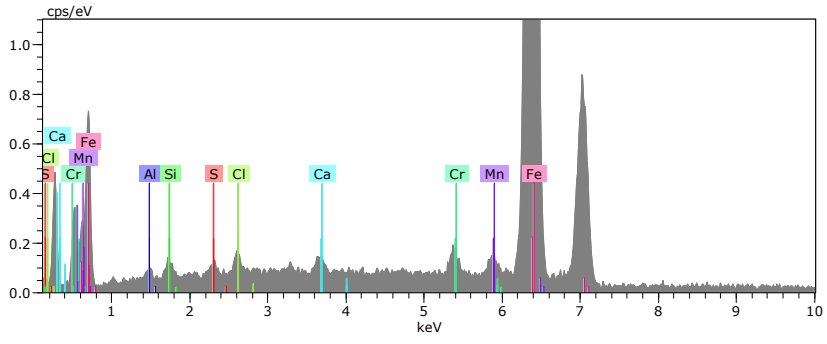
Figure 12. Half-shaft 2 microstructure: (**a**) Olympus PMG3 microscope with ×500 magnification; (**b**) SEM S-2400 with ×2000 magnification.

3.3. Chemical Analysis

A chemical analysis was performed in order to evaluate the different elements that compose the material of the half-shafts. The half-shaft 1 sample's two-zone chemical composition was revealed by the energy dispersive X-ray spectroscopy (EDS) component of the SEM (EDS1 and EDS2). The chemical analysis was obtained from samples taken far from the fracture sections (samples 1E and 2E) of each half-shaft (see Figures 4b and 4d, respectively), see Figure 13a,b. The same was found to be true for the half-shaft 2 sample, see Figure 13c,d, where a chemical composition analysis was performed. Table 1 shows a summary of the chemical compositions of the elements, with information on the locations they were found in both of the half-shafts. Based on the obtained data, it was found that the material corresponds to the AISI 5120 H chromium alloy steel. The condition of the AISI 5120 H steel considered for the comparison results takes into account a heat treatment comprising cementation, reheating at 800 °C, and quenching and tempering at 150 °C.



(**a**)



(**b**)

Figure 13. *Cont.*

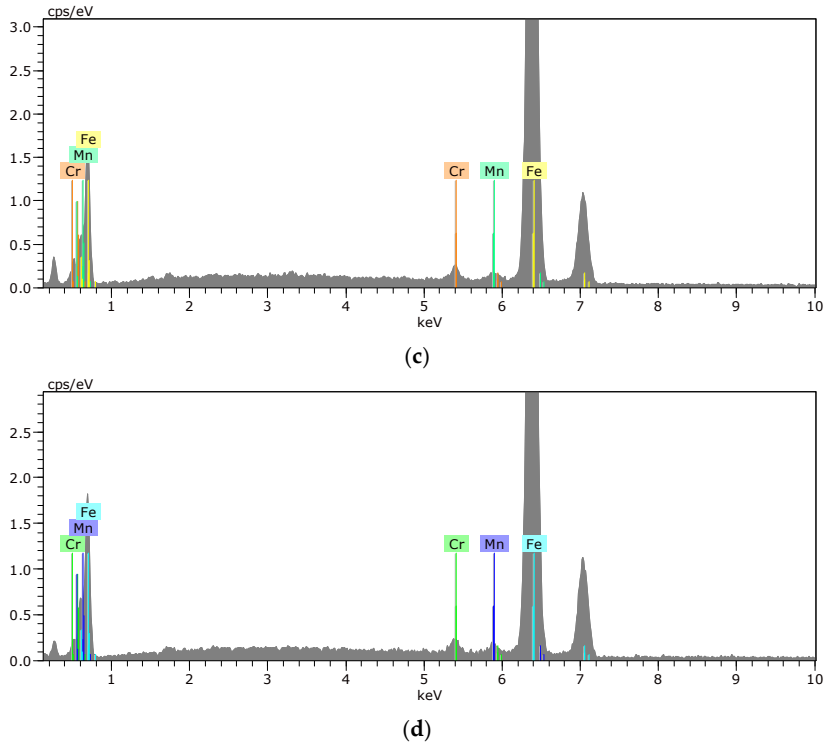


Figure 13. Half-shaft 1 EDS spectrum (**a**) EDS1 and (**b**) EDS2; half-shaft 2 EDS spectrum; (**c**) EDS1 and (**d**) EDS2.

Table 1. Chemical composition of the two sample zones from half-shaft 1 and half-shaft 2 and AISI 5120 H steel (wt.%).

	S 1 (EDS1)	S 1 (EDS2)	S 2 (EDS1)	S 2 (EDS2)	AISI 5120 H
C					0.17–0.22
Al	–	0.29	–	–	–
Cl	–	0.54	0.76	0.74	–
Ca	–	0.56	–	–	–
Si	–	0.39	–	–	0.35 (máx.)
Mn	0.84	0,76	–	–	0.60–1.00
P	–	–	–	–	0.035 (máx.)
S	–	0.37	–	–	≤0.040
Cr	1.00	0.69	1.01	0.94	0.60–1.00
Fe	98.16	96.39	98.22	98.32	Balance

3.4. Mechanical Evaluation of the Material

Tensile tests were performed using samples 1A, 1B, 2A, and 2B (see Figure 4) in order to obtain the main mechanical characteristics of the materials under study. Since the nominal stress–strain curves associated with half-shaft 1 (Figure 14a) are quite similar to half-shaft 2's curves (Figure 14b), it may be inferred that both half-shafts are made of the same material. The lowest value was chosen from each property when assessing the mechanical characteristics of each test specimen, since it is a more cautious strategy than taking into account the average of the data. Table 2 presents the main mechanical properties obtained in the tensile tests of the half-shafts' materials. In Table 2, one can see the mechanical properties of AISI 5120 H steel; for comparison, see the following: the yield strength and ultimate tensile strength are around 700 MPa and 860 MPa (on average), respectively, and the Young's moduli are similar, around 206 GPa. The ductility of the steel was also verified.

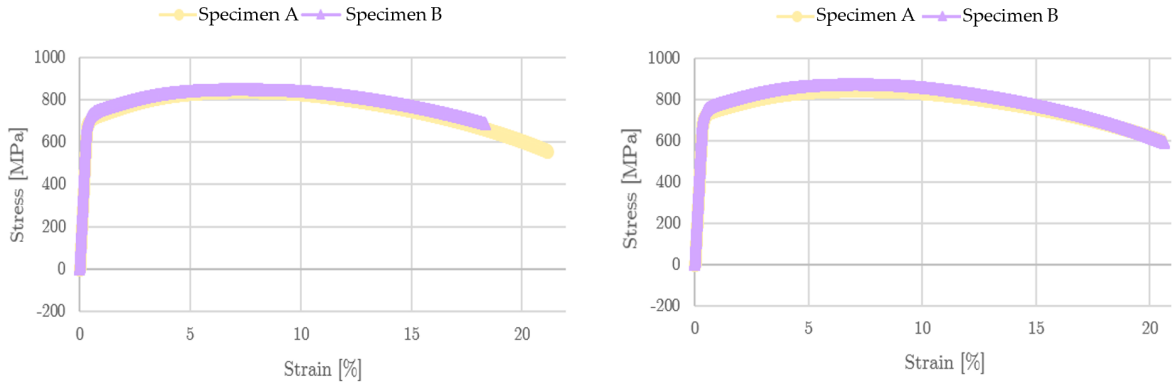


Figure 14. Nominal stress–strain curve of the: (**a**) half-shaft 1—A and B test specimens; (**b**) half-shaft 2—A and B test specimens.

Table 2. Mechanical properties of the material studied in this article and of AISI 5120 H steel.

	$\sigma_e = S_y$ [MPa]	S_{uts} [MPa]	ε_F [%]	E [GPa]
Tested material	701 ± 20	840 ± 20	18 ± 3	206 ± 20
AISI 5120 H	696	883	15	205

4. Computing the Half-Shaft Safety Factor

Two possible scenarios were taken into consideration in an effort to comprehend and quantify the impact of the loading conditions on the mechanical behavior of the half-shafts and, as a result, their safety: Scenario (1)—when the vehicle travels straight ahead; Scenario (2)—when it makes tight turns. These were chosen because these are the two types of road segments that the 3WEV encounters the most frequently. The objective is to characterize and assess the evolution of the stresses in the half-shafts, namely on those sections where the half-shafts fractured. Knowing these data, the determination of the fatigue safety coefficient by two well-known fatigue criteria was performed.

The half-shafts investigated in this work belong to the e-Tuk Limo vehicle [14]; some technical requirements of this vehicle are presented in Table 3. This is a 100% three-wheeled electric vehicle with a capacity of 6 + 1 passengers and with a maximum payload of 300 kg.

Table 3. Technical specifications of the e-Tuk Limo, adapted from [14].

Technical Specifications	
$L \times W \times H$	3890 × 1850 × 1410 mm
Wheelbase	2700 mm
Rear width	1255 mm
Steering angle (measured)	45°
Maximum weight	1030 kg

Considering possible real-world scenarios, the one in which half-shafts are most frequently requested is when the car is making a sharp curve, that is, when the half-shaft is attached to the inner wheel, as illustrated in Figure 15. The forces causing the loads on the half-shaft in this scenario are explained in the follow paragraphs, and the fatigue safety coefficients are then calculated.

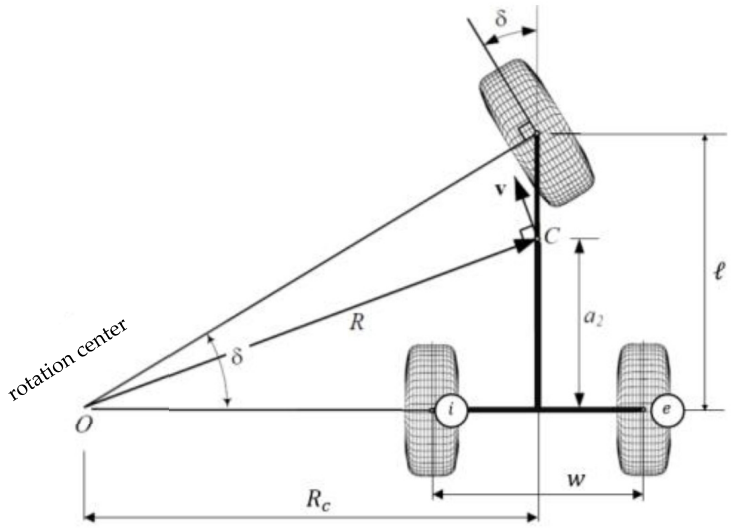


Figure 15. Ackerman's geometry for a three-wheeled vehicle, adapted from [31].

From the analysis of the routes traveled by this vehicle in the city of Lisbon, one can determine that, along the course, there are several tight curves. Accounting for this fact in the following analysis, the assumed curvature radius was deduced based on Ackerman's geometry for a three-wheeled vehicle (Figure 15); here, the distance between the steer axes of the steerable wheels (the track) is represented by w, the distance between the front and rear axles is represented by l, and the steering angle is shown by δ [31].

The center of mass (letter O in Figure 15 is the rotation center) of the vehicle describes a circle of radius, R, and this radius of curvature is perpendicular to the vehicle's speed vector in C. Observing the presented geometry, Equations (1)–(3) were considered, which led to a curvature radius of 3.0 m, according to the mechanical characteristics of the vehicle [31].

$$\tan(\delta) = {}^{\ell}/_{R_c} \Longleftrightarrow R_c = {}^{\ell}/_{\tan(\delta)} = \ell \times \cot(\delta), \tag{1}$$

$$R^2 = {R_c}^2 + {a_2}^2 \Leftrightarrow R = \sqrt{{a_2}^2 + {R_c}^2} = \sqrt{{a_2}^2 + (\ell \times \cot(\delta))^2}, \tag{2}$$

$$R_{int} = R_c - \frac{w}{2}, \tag{3}$$

To determine the speed at which the vehicle should take the curve, a limit situation was considered as a function of the maximum friction between the tire and the road. The vehicle is traveling at 16 km/h (on average for this condition); this means that the power should be one-fourth of the engine's power. It is possible to display and calculate the loads considered on the half-shafts, given the conditions under which the vehicle executes the curve; it is important to note that a movable support was considered at point B (green bearing in Figure 16a) and that a fixed support was considered at point C (purple bearing in Figure 16a).

At point A, the torsion moment connected to the transmission of this force to the half-shaft (T_{F_t}) and the tangential component of the gearing force acting on the planetary gear teeth ($F_t = T$) are shown.

As indicated in Figure 16a, the forces at point D related to the weight carried by the inner wheel (F_D), a lateral force ($F_{lt,i}$), and the bending moment ($M_{F_{lt,i}}$) related to its transmission to the half-shaft. The weight on the outer wheel is often greater than the weight on the inner wheel during turning.

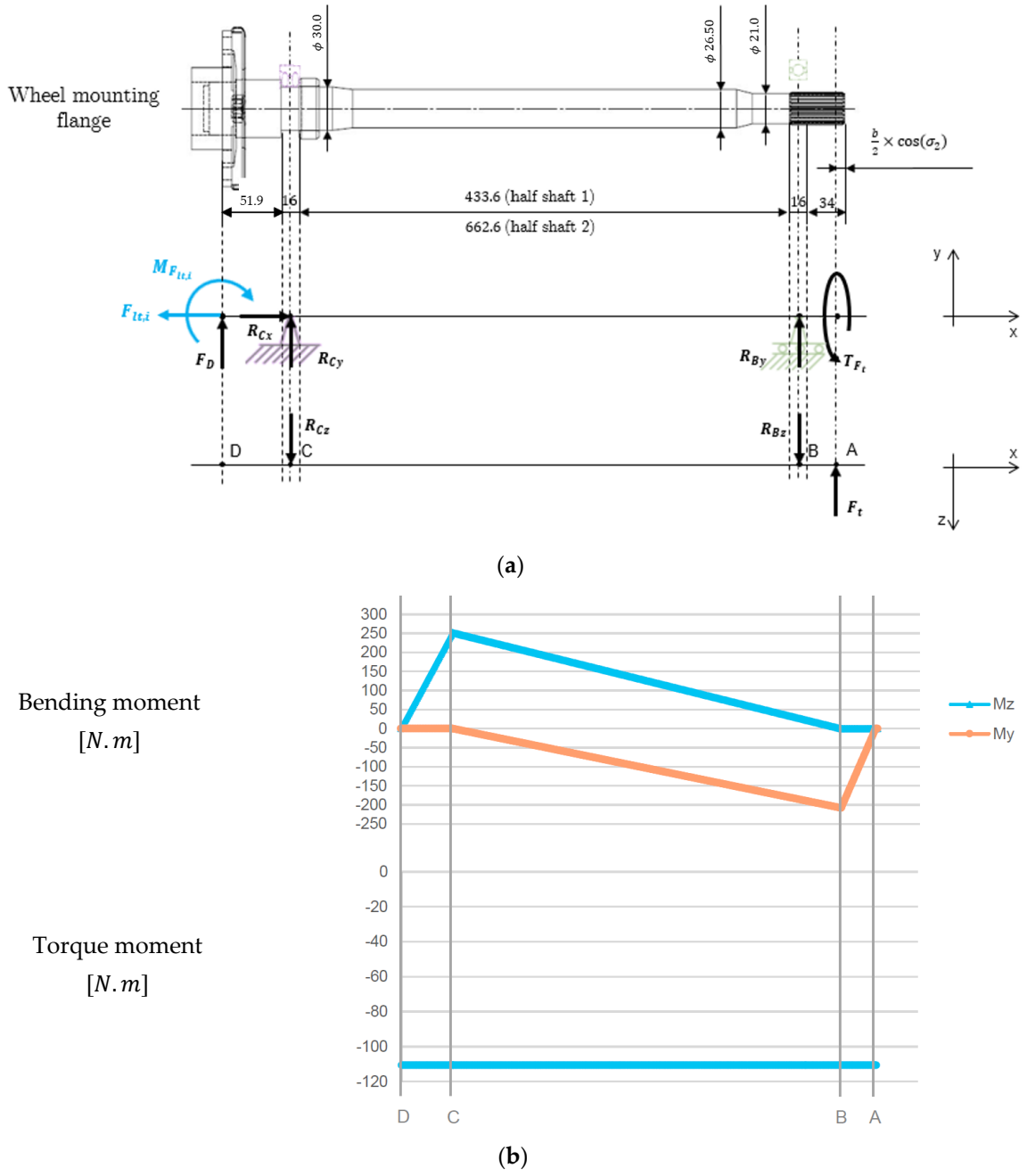


Figure 16. (**a**) Static equilibrium diagram of the half-shaft when it is connected to the inner wheel while cornering (this figure considers the curve to the left of the half-shaft); (**b**) bending moments Mz and My and torque moment diagrams (dimensions in mm).

As a result, 40% of the rear weight was considered to go to the inner wheel and 60% was considered to go to the outer wheel. In Figure 16b, one can see diagrams of the bending moment and the torque moment. The torque moment, based on a power engine, is steady along the half-shaft, with a value of 110 N.m (the negative value presented in Figure 16b accounts for the sense of the loading, which does not influence the final results). The bending moment, M_z, varies along the half-shaft, reaching a maximum at point C (around 250 N.m, M_y is null in this section); this is close to the section where half-shaft 1 reached its failure point. Based on these achievements, one can say that the high applied loading, close to the presence of the diameters' transition, contributed to the failure of the half-shaft.

The lateral force applied to the tire multiplies the weight carried by the wheel by the coefficient of friction; thus, its distribution is the same as the weight distribution on the rear

axle. The centrifugal force exerted on the vehicle's center of mass serves as the basis for calculating this lateral force.

The responses on the supports were computed using the balance of forces and moments using the applied forces and moments at points A and D as input; as a result, the stresses in the fractured portions were determined.

Safety Check of Studied Components

Based on the computed loading, one can identify that it represents a non-fully reversed fatigue loading cycle. Therefore, to perform the fatigue calculations, i.e., to determine the fatigue safety factor, the modified Goodman criterion (4) and the ASME–elliptic criterion (5) should be considered [32]:

$$\frac{\sigma_a}{S_e} + \frac{\sigma_m}{S_{ut}} = \frac{1}{n} \tag{4}$$

$$\left(\frac{n \times \sigma_a}{S_e}\right)^2 + \left(\frac{n \times \sigma_m}{S_y}\right)^2 = 1 \tag{5}$$

where σ_a (half-shaft 1 = 207 MPa; half-shaft 2 = 409 MPa) and σ_m (half-shaft 1 = 73 MPa; half-shaft 2 = 29 MPa) correspond to alternating and midrange stresses, respectively; S_e is endurance limit stress (250 MPa); S_{ut} and S_y are the ultimate tensile strength and the yield strength of the material under study, respectively.

In the determination of the alternating and mean stresses, the equivalent von Mises approach was considered, taking into account the stress distribution associated with each effort in the critical section. As half-shaft 1 fractured in a transition zone of diameters, there was a need to correct the stresses by the fatigue stress concentration factor.

Knowing the loading, i.e., the alternating and mean stresses, the considering a fatigue limit for 10^6 cycles and material characteristics, the fatigue safety coefficient associated with each criterion was calculated (please see Table 4). As can be observed from Table 4, regarding half-shaft 1, the safety factors are greater than 1, but very marginally; for half-shaft 2, both the results computed by modified Goodman criterion and those computed by the ASME–elliptic criterion are below 1. Therefore, both criteria present very-low- or no-safety factors for the loading conditions studied.

Table 4. Fatigue safety coefficients of each half-shaft.

	Modified Goodman	**ASME–Elliptic**
Half-shaft 1	1.09	1.19
Half-shaft 2	0.60	0.68

Accounting for the uncertainty surrounding the factors that influence a fatigue failure—particularly in the present study, where various factors should be accounted for, such as the type of pavement (which is full of bumps due to the nature of Portuguese paving), the course of the circuits (which include hill climbs with different slopes), and the number of passengers to be transported (sometimes a higher number than that established by law)—the study carried out here leads to the conclusion that the design of the mechanical components should be improved.

5. Conclusions and Recommendations

This study evaluated and examined the failure of two half-shafts of unknown material belonging to an electric vehicle (Tuk Tuk). Comprehensive analyses, including tensile testing, metallographic examination, chemical composition, and fracture surface, were conducted on samples from both half-shafts. Based on the investigations performed regarding the half-shafts, the following conclusions can be drawn:

1. The half-shafts are made from the same material, which is a chromium alloy steel, and this is an adequate steel for this type of component.

2. Both half-shafts failed due to fatigue damage, based on the fractographic evidence in different samples.
3. Fatigue criteria were applied; these confirmed that the computed safety factor is below or around 1.0, which means the design of the half-shafts of these vehicles needs some improvements for the real loading service conditions in which they are operating.

In order to improve the operating conditions and consequently the safety of these type of mechanical components, several aspects should be taken into account:

- The material to be used in its manufacture should be certified.
- The manufacture of the half-shafts should correctly follow the respective technical drawings; additional care should be taken in designing the transition zones of the diameters.
- The maximum permitted payload for the transport of passengers must never be exceeded.
- During a journey, the accelerations and velocities achieved must not exceed those outlined in regulation.
- Since the Tuk Tuk is an electric vehicle, drivers must start the vehicle in a non-abrupt way every time, i.e., the start should be performed smoothly until the cruising speed is reached.
- A safety factor of at least 1.5 should be assured for this type of mechanical component.

Author Contributions: Conceptualization, J.H.L., I.M., E.M.A. and L.R.; methodology, I.M. and L.R.; validation, I.M. and L.R.; formal analysis, I.M. and L.R.; investigation, J.H.L., I.M. and L.R.; resources, L.R. and E.M.A.; writing—original draft preparation, I.M. and J.H.L.; writing—review and editing, L.R., E.M.A. and I.M.; supervision, L.R. and E.M.A.; funding acquisition, L.R. All authors have read and agreed to the published version of the manuscript.

Funding: The authors acknowledge Fundação para a Ciência e a Tecnologia (FCT) for its financial support via the project LAETA Base Funding (https://doi.org/10.54499/UIDB/50022/2020).

Data Availability Statement: The raw data supporting the conclusions of this article will be made available by the authors on request.

Acknowledgments: Authors would like to thank to the TUK ON ME company, to Henrique Soares for his contribution, to the preparation of samples for metallographic analysis and hardness measurements.

Conflicts of Interest: The authors declare no conflict of interest.

References

1. Hou, N.; Ding, N.; Qu, S.; Guo, W.; Liu, L.; Xu, N.; Tian, L.; Xu, H.; Chen, X.; Zaïri, F.; et al. Failure Modes, Mechanisms and Causes of Shafts in Mechanical Equipment. *Eng. Fail. Anal.* **2022**, *136*, 106216. [CrossRef]
2. Zhao, L.H.; Xing, Q.K.; Wang, J.Y.; Li, S.L.; Zheng, S.L. Failure and Root Cause Analysis of Vehicle Drive Shaft. *Eng. Fail. Anal.* **2019**, *99*, 225–234. [CrossRef]
3. Ahsan Feroz, A.; Harshit; Chawla, D.; Kumar, R. To Study and Analyze the Design of Drive Shafts for Automobiles Using Composite Material through Empirical Review on Literature. *Mater. Today Proc.* **2022**, *56*, 3820–3822. [CrossRef]
4. Johnson, M.S.; Evans, R.; Mistry, P.J.; Li, S.; Bruni, S.; Bernasconi, A.; Cervello, S. Structural Analysis for the Design of a Lightweight Composite Railway Axle. *Compos. Struct.* **2022**, *290*, 115544. [CrossRef]
5. Jarrett, W.; Jeffs, S.P.; Korkees, F.; Rawson, M. The Opportunities and Challenges of Hybrid Composite Driveshafts and Their Couplings in the Aerospace Industry: A Review. *Compos. Struct.* **2023**, *320*, 117203. [CrossRef]
6. Johanson, C.; Duffy, J.E. Rear Axle Assembly Construction and Operation. In *Manual Drive Trains and Axles*, 3rd ed.; Goodheart-Willcox: Chicago, IL, USA, 2015; pp. 309–333.
7. Asi, O. Fatigue failure of a rear axle shaft of an automobile. *Eng. Fail. Anal.* **2006**, *13*, 1293–1302. [CrossRef]
8. Bayrakceken, H.; Tasgetiren, S.; Yavuz, I. Two Cases of Failure in the Power Transmission System on Vehicles: A Universal Joint Yoke and a Drive Shaft. *Eng. Fail. Anal.* **2007**, *14*, 716–724. [CrossRef]
9. Verma, R.P.; Singh, M.; Lila, M.K. Failure Prediction of Rear Axle of a Three Wheeler Vehicle by Dynamic Analysis: Computational Approach. *Mater. Today Proc.* **2021**, *46*, 10896–10903. [CrossRef]
10. Barone, C.; Casati, R.; Dusini, L.; Gerbino, F.; Guglielmino, E.; Risitano, G.; Santonocito, D. Fatigue Life Evaluation of Car Front Halfshaft. *Procedia Struct. Integr.* **2018**, *12*, 3–8. [CrossRef]

11. Guimaraes, A.V.; Brasileiro, P.C.; Giovanni, G.C.; Costa, L.R.O.; Araujo, L.S. Failure Analysis of a Half-Shaft of a Formula SAE Racing Car. *Case Stud. Eng. Fail. Anal.* **2016**, *7*, 17–23. [CrossRef]
12. Alberti, F.; Foti, P.; Berto, F.; Risitano, G.; D'Andrea, D. Fatigue Life Evaluation of Automotive Mechanical Components by Using Smart Design Algorithm. *Fatigue Fract. Eng. Mater. Struct.* **2023**, *46*, 1401–1412. [CrossRef]
13. *ASM Handbook—Metals Handbook, Volume 12—Fractography*, 9th ed.; ASM International: Materials Park, OH, USA, 1987.
14. de Branco, C.A.G. *Mecânica dos Materiais*, 5th ed.; Fundação Calouste Gulbenkian: London, UK, 2011.
15. Vicente, C.; Sardinha, M.; Reis, L. Failure analysis of a coupled shaft from a shredder. *Eng. Fail. Anal.* **2019**, *103*, 384–391. [CrossRef]
16. Fonte, M.; Freitas, M.; Reis, L. Failure analysis of a damaged diesel motor crankshaft. *Eng. Fail. Anal.* **2019**, *102*, 1–6. [CrossRef]
17. Fonte, M.; Reis, L.; Infante, V.; Freitas, M. Failure analysis of cylinder head studs of a four-stroke marine diesel engine. *Eng. Fail. Anal.* **2019**, *101*, 298–308. [CrossRef]
18. Bonnett, A.H. Root Cause AC Motor Failure Analysis with a Focus on Shaft Failures. *IEEE Trans. Ind. Appl.* **2000**, *36*, 1435–1448. [CrossRef]
19. Li, Y.J.; Zhang, W.F.; Tao, C.H. Fracture Analysis of a Castellated Shaft. *Eng. Fail. Anal.* **2007**, *14*, 573–578. [CrossRef]
20. Yu, Z.W.; Xu, X.L.; Yang, Z.; Li, Y.Y. Case Internal Oxidation and Intergranular Fracture of Carburized Splined-Shaft. *Eng. Fail. Anal.* **2012**, *22*, 141–151. [CrossRef]
21. Liu, Y.; Lian, Z.; Xia, C.; Qian, L.; Liu, S. Fracture Failure Analysis and Research on Drive Shaft of Positive Displacement Motor. *Eng. Fail. Anal.* **2019**, *106*, 104145. [CrossRef]
22. Bi, T.T.; Yang, Z.G. Failure Analysis on Speed Reducer Shaft of Sluice Gate in Nuclear Power Plant. *Eng. Fail. Anal.* **2017**, *80*, 453–463. [CrossRef]
23. Xu, L.; Yu, X.; Hou, Z. Analysis of the Causes of Driving Gear Shaft Fractures in Gear Pumps. *J. Fail. Anal. Prev.* **2020**, *20*, 242–248. [CrossRef]
24. Kumar, L. Study on the Front Axle and Rear Axle Attached to Differential System. *Int. J. Innov. Res. Sci. Technol.* **2014**, *1*, 9–12.
25. Das, S.; Mukhopadhyay, G.; Bhattacharyya, S. Failure Analysis Failure analysis of axle shaft of a fork lift. *Case Stud. Eng. Fail. Anal.* **2015**, *3*, 46–51. [CrossRef]
26. Nyberg, C. Understanding Factors That Cause Shaft Failures. *Pumps Syst. June* **2007**, 24–27.
27. Dowling, N.E. *Mechanical Behavior of Materials—Engineering Methods for Deformation, Fracture, and Fatigue*, 4th ed.; Pearson: San Francisco, CA, USA, 2012.
28. Fajdiga, G.; Glodež, S.; Kramar, J. Pitting formation due to surface and subsurface initiated fatigue crack growth in contacting mechanical elements. *Wear* **2007**, *262*, 1217–1224. [CrossRef]
29. eTuk Factory. Available online: https://etukfactory.com/limo (accessed on 9 June 2020).
30. *ASTM E8/E8M-16a*; Standard Test Methods for Tension Testing of Metallic Materials. ASTM International: West Conshohocken, PA, USA, 2016.
31. Jazar, R.N. *Vehicle Dynamics—Theory and Application*; Springer: Berlin/Heidelberg, Germany, 2008.
32. Budynas, R.G.; Nisbett, J.K. *Shigley's Mechanical Engineering Design*, 10th ed.; McGraw-Hill Education: Berlin/Heidelberg, Germany, 2015.

Disclaimer/Publisher's Note: The statements, opinions and data contained in all publications are solely those of the individual author(s) and contributor(s) and not of MDPI and/or the editor(s). MDPI and/or the editor(s) disclaim responsibility for any injury to people or property resulting from any ideas, methods, instructions or products referred to in the content.